Journal of Ceramic Processing Research. Vol. 26, No. 3, pp. 386~396 (2025)
(Received 18 December 2024, Received in revised form 17 February 2025, Accepted 28 February 2025)
https://doi.org/10.36410/jcpr.2025.26.3.386

JOURNAL OF
Ceramic Processing Research

Reactive ultrafast high-temperature sintering of $(La_{0.2}Gd_{0.2}Sm_{0.2}Eu_{0.2}M_{0.2})_2Zr_2O_7$ (M=Y or Yb) high-entropy ceramics

Jiahang Liu[a], Zhe Lu[a,*], Yeon-Gil Jung[b,*], Yan Li[a], Yanwen Zhou[a], Hao Chen[c], Jeong-Hun Son[b], Heekyu Choi[b] and Jun-Seob Lee[b]

[a]*School of Materials and Metallurgical Engineering, University of Science and Technology Liaoning, Anshan 114051, China*
[b]*School of Materials Science and Engineering, Changwon National University, Changwon, Gyeongnam 641773, Republic of Korea*
[c]*Shandong Nuclear Power Equipment Manufacturing Co., Ltd, Haiyang 265100, China*

In the present work, a single-phase $(La_{0.2}Gd_{0.2}Sm_{0.2}Eu_{0.2}Y_{0.2})_2Zr_2O_7$ (LGSEY) high-entropy ceramic with pyrochlore structure and a dual-phase $(La_{0.2}Gd_{0.2}Sm_{0.2}Eu_{0.2}Yb_{0.2})_2Zr_2O_7$ (LGSEYb) high-entropy ceramic with co-existing pyrochlore and fluorite structure were designed by cation radius differences and successfully synthesized by reactive ultrafast high-temperature sintering (RUHS). The synthesis was completed in less than 1 h, demonstrating the efficiency of the RUHS technique for preparing complex high-entropy $Re_2Zr_2O_7$ ceramics. XRD results showed that RUHS could synthesize high-entropy $Re_2Zr_2O_7$ with a specified phase composition. TEM and SEM confirmed the uniform distribution of rare-earth elements in the ceramics, minimizing compositional bias and enhancing material properties. Both ceramics exhibited low thermal conductivity due to significant lattice distortion, with LGSEYb displaying an amorphous thermal conductivity. In addition, the inherent cationic radius differences and lattice distortions in high-entropy ceramics contribute to the low Young's modulus and high hardness. Finally, both ceramics exhibit excellent high-temperature phase stability from room temperature to 1500 °C. This work highlights the potential of RUHS for synthesizing high-entropy ceramics with complex structures and provides valuable insights for optimizing their use in thermal barrier coatings.

Keywords: Ultrafast high-temperature sintering, High-entropy ceramic, Structure, Thermal conductivity, Mechanical properties.

Introduction

As a crucial component of aviation aircraft, the development trend of aero-engines mainly focuses on improving the thrust-to-weight ratio, fuel efficiency, and service life extension [1]. The performance improvements significantly rely on the capabilities of the hot-end components, particularly the high-temperature resistance of the turbine blades and rotor blades [2]. Thermal barrier coatings (TBCs) have a significant impact on the development of advanced aero-engines due to the ability to effectively protect critical hot-end components of advanced turbine engines, extend the service life, and improve fuel efficiency [3-5]. A conventional TBC comprises three main parts, including a ceramic top coat (TC), a metal bond coat (BC), and a superalloy substrate [6]. Among them, the TC is designed to endure a high-temperature service environment. Therefore, it must have superior thermal insulation and high-temperature phase stability [7]. Currently, traditional YSZ is the most used ceramic material for TBCs due to its relatively superior thermophysical properties [8]. However, with the continuous development of aero-engines, the service temperature of hot-end components has exceeded 1500 °C [9]. At such temperatures, the YSZ will exhibit phase transformation and sintering, weakening the insulation performance and service life of TBCs [10]. Therefore, developing new TBC ceramic materials that can replace YSZ is urgently needed.

In recent years, the application of ceramic materials such as perovskite structure caramic ($SrZrO_3$), rare-earth tantalates ($ReTaO_4$), lanthanum magnesium hexaaluminate ($LaMgAl_{11}O_{19}$), and rare-earth zirconates ($Re_2Zr_2O_7$) in TBCs has gradually increased [11-14]. Among them, $Re_2Zr_2O_7$ is considered to be the next-generation ceramic material for TBCs owing to its superior high-temperature phase stability and thermal insulation properties [15]. However, the thermodynamic properties of $Re_2Zr_2O_7$ are relatively weak, leading to unsatisfactory performance in practical applications [16]. Therefore, it is important to further optimize $Re_2Zr_2O_7$.

In 2004, Yeh et al. [17] designed and synthesized a multicomponent doped alloy and proposed the concept

---

*Co-correspond authors:
Zhe Lu
Tel: +86-15941242356
E-mail: lz19870522@126.com
Yeon-Gil Jung
Tel: 055-213-3712
E-mail: jungyg@changwon.ac.kr

of high-entropy. In 2015, Rost et al. [18] introduced this concept to ceramic materials. Several investigations have shown that the introduction of high-entropy effects in $Re_2Zr_2O_7$ can optimize their performance [19-22]. In recent years, introducing a dual-phase structure in high-entropy $Re_2Zr_2O_7$ is a new method to optimize the properties of $Re_2Zr_2O_7$ ceramics. Wang et al. [23] prepared high-entropy $Re_2Zr_2O_7$ composed of different components. They verified that the formation mechanism of dual-phase high-entropy $Re_2Zr_2O_7$ was not related to entropy but was determined by enthalpy and size disorder by comparing the configurational entropy and size disorder among different materials. Zhu et al. [24] designed and synthesized $(La_{0.2}Nd_{0.2}Y_{0.2}Er_{0.2}Yb_{0.2})_2Zr_2O_7$ ceramics with dual-phase structure by conventional solid-phase reaction method, and the large size disorder made it exhibit an amorphous thermal conductivity. However, significant compositional segregation was observed in $(La_{0.2}Nd_{0.2}Y_{0.2}Er_{0.2}Yb_{0.2})_2Zr_2O_7$. Shuai et al. [25] synthesized a dual-phase high-entropy $(La_{0.2}Nd_{0.2}Gd_{0.2}Er_{0.2}Yb_{0.2})_2Zr_2O_7$ ceramic with amorphous thermal conductivity by co-precipitation and conventional solid-phase reaction method. However, $(La_{0.2}Nd_{0.2}Y_{0.2}Er_{0.2}Yb_{0.2})_2Zr_2O_7$ ceramics prepared by co-precipitation exhibit different phase transformation behavior at various sintering temperatures. In summary, the ceramic synthesis methods affect the phase composition and thermal properties of high-entropy $Re_2Zr_2O_7$.

In 2020, Wang et al. [26] successfully developed the ultrafast high-temperature sintering (UHS) technique and applied this technique to the ultrafast synthesis of YSZ [27], $Li_{6.5}La_3Zr_{1.5}Ta_{0.5}O_{12}$ [28], ZrC-based ceramics [29], and $NaNbO_3$ materials [30]. Compared to the conventional solid-phase reaction method, UHS technology has a high-speed heat-up rate and high sintering temperatures, allowing the synthesis of ceramic samples in a short time [31]. However, the synthesis of single-phase and dual-phase high-entropy $Re_2Zr_2O_7$ by UHS has rarely been reported.

In the present work, high-entropy $(La_{0.2}Gd_{0.2}Sm_{0.2}Eu_{0.2}Y_{0.2})_2Zr_2O_7$ (LGSEY) and $(La_{0.2}Gd_{0.2}Sm_{0.2}Eu_{0.2}Yb_{0.2})_2Zr_2O_7$ (LGSEYb) was designed and synthesized by reactive ultrafast high-temperature sintering (RUHS). The entire sintering process was completed in less than 1 h, demonstrating the feasibility of the RUHS technique in the rapid synthesis of single-phase and dual-phase high-entropy $Re_2Zr_2O_7$. On this basis, the phase composition, structural characterization, and elemental distributions of LGSEY and LGSEYb were characterized. In addition, the thermal conductivity, mechanical properties, and phase stability of the two high-entropy ceramics were explored.

Experimental Procedure

Composition design

Composition design is a key factor determining the phase composition, crystal structure, and properties of high-entropy ceramics applied to thermal barrier coatings. The LGSEY and LGSEYb designed in this work represent single-phase and dual-phase high-entropy $Re_2Zr_2O_7$, respectively. Based on the difference in Shannon ion radius and excellent modification ability, Gd^{3+}, Sm^{3+}, and Eu^{3+} were selected as the modified rare-earth elements and doped at the Re site. Among them, the elements Sm^{3+} and Eu^{3+} have been proven to be more likely to form substitution defects and oxygen vacancies during the preparation of high-entropy ceramics, which is favorable to reducing the thermal conductivity of high-entropy ceramics [32, 33]; The element Gd^{3+} has been proven to favor the formation of defect-fluorite micro-domains during the preparation of high-entropy ceramics, and increasing the degree of lattice disorder within the high-entropy ceramics [34]. As a unique lanthanide element, although Y^{3+} has a Shannon ion radius similar to that of Eu^{3+}, its relative atomic mass is only 88.9, so the selection of element Y^{3+} to be doped at the RE site is favorable to increase the mass difference of high-entropy ceramics and reduce the thermal conductivity. Yb^{3+} has different properties from Y^{3+}. Yb^{3+} is the lanthanide element with the largest relative atomic mass and the smallest Shannon ion radius, so the selection of Yb^{3+} for doping at the Re site is favorable to increase the size difference within the high-entropy ceramics, which affects the phase composition as well as the thermal properties.

After designing the composition of LGSEY and LGSEYb, the phase compositions of the two high-entropy ceramics were predicted. The formation mechanism of dual-phase high-entropy LGSEYb can be described according to the size disorder (δ) proposed by Wang et al., which can be calculated as [23]:

$$\delta = \sqrt{\sum_{i=1}^{N} X_i \left(1 - \frac{r_i}{\sum_{i=1}^{N} X_i r_i}\right)^2} \times 100\% \tag{1}$$

where N is the number of rare-earth cation species, X_i is the molar fraction, and r_i is the Shannon ionic radius of the i-th element in rare-earth cations. Fan and Yang et al. [35, 36] designed dual-phase $Re_2Zr_2O_7$ ceramics based on the ionic radius and found that $Re_2Zr_2O_7$ preferred to form a dual-phase structure when the R_A/R_B was between 1.4-1.5 and the $\delta > 5.2\%$. Based on the Table 1, the R_A/R_B of LGSEY and LGSEYb were 1.4936 and 1.467, respectively. The δ of LGSEY and LGSEYb were 4.35% and 5.85%, respectively. Therefore, the LGSEY and LGSEYb designed in this work should have a single-phase and dual-phase structure, respectively.

Sample preparation and characterization

The commercially available La_2O_3, Gd_2O_3, Sm_2O_3, Eu_2O_3, Y_2O_3, Yb_2O_3, and ZrO_2 (99.9 wt% purity, Shanghai Yaotian, China) were used as raw materials.

Table 1. Oxidation state, coordination number, relative atomic mass, and Shannon ion radius of elements.

Symbols for elements	La	Gd	Sm	Eu	Y	Yb	Zr	O
Oxidation state	+3	+3	+3	+3	+3	+3	+4	-2
Coordination number (CN)	VIII	VIII	VIII	VIII	VIII	VIII	VI	VI
Relative atomic mass (*Mi*)	138.9	157.2	150.4	151.9	88.9	173	91.2	16
Shannon ion radius (pm)	116	105.3	107.9	106.6	101.9	98.5	72	140

Firstly, the rare-earth oxides and ZrO_2 were accurately weighed and mixed according to a preset molar ratio. Secondly, the mixed powders were ball-milled for 15 h at 400 rpm using ZrO_2 balls as milling media and absolute ethyl alcohol as carrier solution. Thirdly, the homogeneously mixed powder was dried at 60 °C for 24 h to remove the absolute ethyl alcohol. The dried powder was molded (60 MPa) and cold isostatically pressed (290 MPa) to obtain ceramic green bodies. Finally, the green bodies were sintered by UHS (UHS-3000, Tianjin Zhonghuan Electric Furnace Co., Ltd, China) at 1800 °C for 5 min with a heating rate of 100 °C/min. Fig. 1 shows the internal structure and schematic diagram of the UHS. Before sintering, the green bodies need to be placed in the center of the graphite felt and sintered under Ar environment.

The phase composition of LGSEY and LGSEYb was characterized by X-ray diffractometer (XRD, PANalytical, Netherlands), and the Rietveld refinements were performed by FullProf software. Transmission electron microscopy (TEM, Talos F200X, USA) was used to characterize the structures and chemical compositions of ceramic materials. The microstructure and elemental distribution were investigated via scanning electron microscopy (SEM, Thermo Scientific, Quattro). The calculated density (ρ_0) was calculated based on the lattice parameters, and the actual density (ρ) was measured by the Archimedes method. The specific heat capacity (C_p) and thermal diffusivity (α) were measured by a laser flash analyzer, and the thermal conductivity (k) was calculated as Eq. (2) [34].

$$k_0 = \frac{3C_p\alpha\rho\rho_0}{4\rho - \rho_0} \tag{2}$$

The Young's modulus (E) was measured by an Ultrasonic reflection device (UMS-100, TECLAB, France) [8]:

$$E = \frac{\rho V_T^2\left(3V_L^2 - 4V_T^2\right)}{\left(V_L^2 - V_T^2\right)} \tag{3}$$

where V_T and V_L represent the transverse and longitudinal acoustic velocities, respectively. The Vickers hardness (H_v) was estimated by using an automatic Vickers microhardness tester (Qness 60 A+ EVO) at 9.8 N for 20 s. The fracture toughness (K_{IC}) was calculated based on the Vickers indentation according to Eq. (4) [25]:

$$K_{IC} = 0.16H_V a^2 c^{-3/2} \tag{4}$$

where a and c represent the half-length of the indent diagonal and crack, respectively.

The phase stability of LGSEY and LGSEYb was analyzed using a synchronous thermal analyzer (TG-DSC, Netzsch STA 449 F3 Jupiter, Germany) from room temperature to 1500 °C with a heating rate of 10 °C/min. The samples were placed in Al_2O_3 crucibles, and the testing environment was argon gas. To determine the phase stability of ceramic materials during long-term calcination at high temperatures, LGSEY and LGSEYb were calcined at 1500 °C for 50 h. Then the XRD was used to characterize the phase composition of the calcined samples.

Results and Discussion

Phase composition

Fig. 2(a) exhibits the XRD patterns of LGSEY, LGSEYb, and the standard PDF cards of the corresponding single component $Re_2Zr_2O_7$. Since LGSEY and LGSEYb

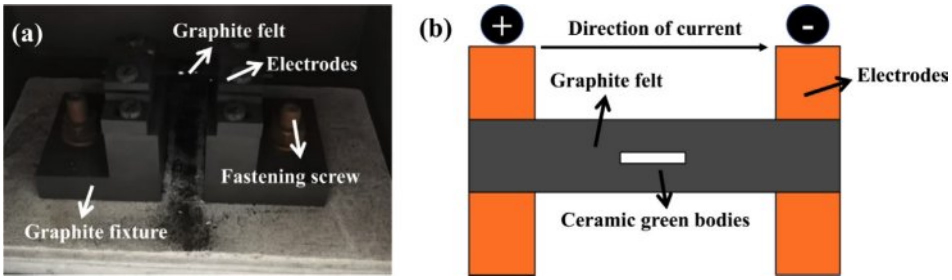

Fig. 1. (a) The heating platform structure of the UHS equipment; (b) The schematic diagram of the UHS equipment.

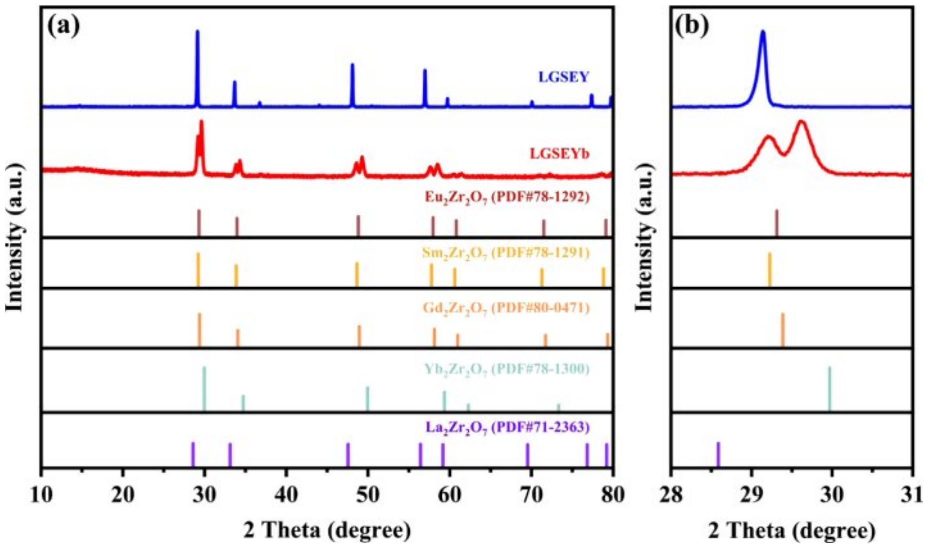

Fig. 2. (a) XRD patterns of LGSEY and LGSEYb, (b) magnified XRD patterns around 29°.

are two new ceramic materials, there are no standard PDF cards for comparison. It could be found that the XRD diffraction peaks of LGSEY were similar to those of $La_2Zr_2O_7$, indicating that the synthesized LGSEY had a single-phase pyrochlore structure. Fig. 2(b) shows the magnified XRD patterns around 29°, the diffraction peaks of LGSEYb were divided into two groups, indicating that the synthesized LGSEYb exhibited a dual-phase structure. In general, the phase composition of single-phase $A_2B_2O_7$ oxide is dependent on the ratio of cation radius at the A and B-sites (R_A/R_B) since the cation radius affects the degree of disorder in the crystal structure. When the R_A/R_B is between 1.46 and 1.78, single-phase $A_2B_2O_7$ tends to form a pyrochlore structure [37]. According to the Shannon ion radius lists in Table 1, the R_A/R_B of LGSEY was 1.4936, which was higher than 1.46. Thus, LGSEY synthesized by RUHS had a pyrochlore structure.

Fig. 3(a) and (b) present the Rietveld refinement curves of LGSEY and LGSEYb. The corresponding refinement results are listed in Table 2. The fitting factors R_{wp} and R_p of all oxides were below 10% and 3%, respectively, indicating high accuracy of the refinement results. The refinement results indicated the LGSEY exhibited a single-phase pyrochlore structure with an Fd-3m space group. Meanwhile, the refinement results indicated the LGSEYb exhibited a dual-phase structure with 56.16% fluorite structure and 43.84% pyrochlore structure. Based on the refinement results, the calculated density of LGSEY was 6.27 g·cm^{-3}. And the calculated density of pyrochlore and fluorite structure of LGSEYb were 6.58 g·cm^{-3} and 6.95 g·cm^{-3}, respectively. Fig. 4(a) and (b) illustrate the relationship between the Re^{3+} cation radius and lattice parameters of LGSEY and LGSEYb. In the pyrochlore structure, the lattice parameters of $La_2Zr_2O_7$ (10.811 Å), $Nd_2Zr_2O_7$ (10.746 Å), $Sm_2Zr_2O_7$ (10.704 Å), LGSEY (10.682 Å), and LGSEYb (10.663 Å) decreased progressively

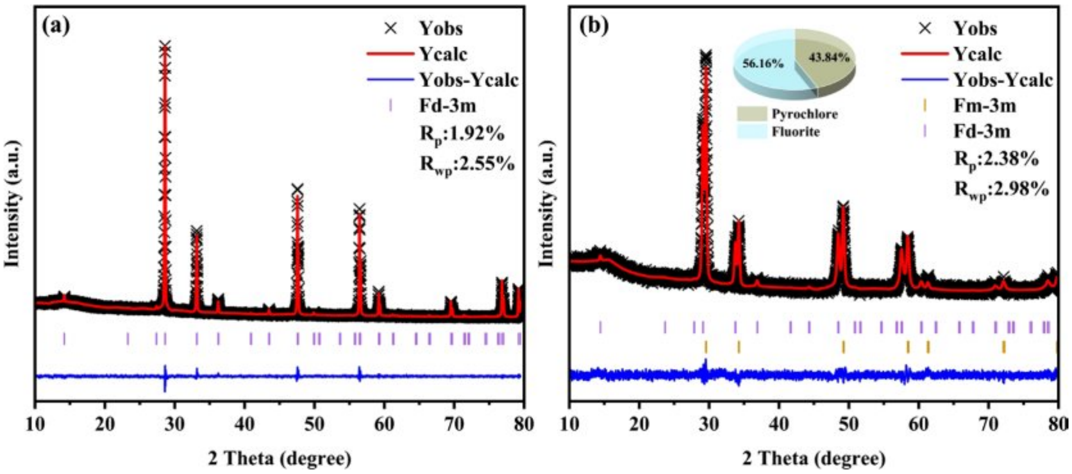

Fig. 3. Rietveld refinement of (a) LGSEY and (b) LGSEYb.

Table 2. Refinement results from the Rietveld refinement of the XRD patterns for LGSEY and LGSEYb. (*Wyck.*: Wyckoff positions; *s.o.f.*: site occupancy factor)

Samples	$a = b = c$ (Å), $\alpha = \beta = \gamma = 90°$									R_{wp}	R_p
	Space group	Atom	Atom positions			*Wyck.*	s.o.f.	a (Å)	V (Å^3)		
			x	y	z						
LGSEY	Fd-3m (227)	Re1	0.5	0.5	0.5	16d	1	10.682	1218.87	2.12	1.71
		Gd2	0	0	0	16c	1				
		O3	0.3342	0.125	0.125	48f	1				
		O4	0.375	0.375	0.375	8b	1				
LGSEYb	Fd-3m (227)	Re1	0.5	0.5	0.5	16d	1	10.663	1187.98	2.38	2.98
		Gd2	0	0	0	16c	1				
		O3	0.3359	0.125	0.125	48f	1				
		O4	0.375	0.375	0.375	8b	1				
	Fm-3m (225)	Re1	0	0	0	4a	0.5	5.288	145.37		
		Zr2	0	0	0	4a	0.5				
		O3	0.25	0.25	0.25	8c	0.875				

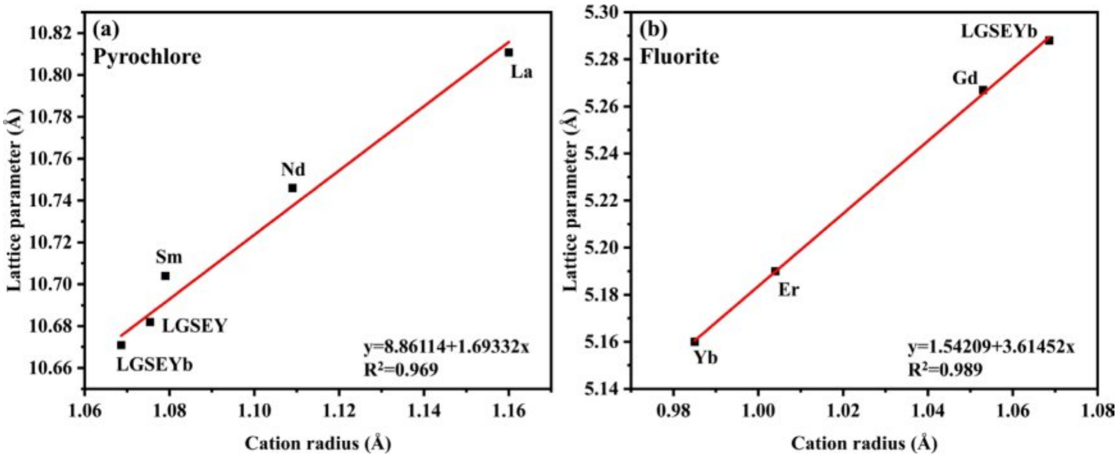

Fig. 4. Lattice parameters of LGSEY and LGSEYb: (a) Pyrochlore and (b) fluorite structure.

as the decrease of the cation radius, demonstrating a linear relationship (y=8.86114+1.69332x). In the fluorite structure, the lattice parameters of $Yb_2Zr_2O_7$ (5.160 Å), $Er_2Zr_2O_7$ (5.191 Å), $Gd_2Zr_2O_7$ (5.270 Å), and LGSEYb (5.288 Å) gradually increased with the increase of the cation radius, exhibiting a clear linear relationship (y=1.54209+3.61452x).

Structural characterization

TEM analysis was used to observe the microstructure further. Fig. 5(a) shows the high-angle annular dark-field (HAADF) image of LGSEY and the corresponding EDS mapping of rare-earth elements. The uniform distribution of all rare-earth elements without significant segregation indicated that RUHS could synthesize single-phase high-entropy $Re_2Zr_2O_7$ with uniform composition. The high-resolution transmission electron microscopy (HRTEM) images of LGSEY are shown in Fig. 5(b) and (c), respectively. The lattice stripe corresponded to the (222) plane, which had a calculated planar spacing of 0.3048 nm. Fig. 5(d) presented the selected area electron diffraction (SAED) pattern of pyrochlore structure that corresponded to the (-440), (-331), and (-222) facets. Fig. 5(e) shows the crystal structure diagram of LGSEY, where the rare-earth elements and Zr^{4+} were randomly and uniformly distributed at positions 16c and 16d, respectively.

Fig. 6(a) presents the HAADF image of the LGSEYb and the corresponding EDS mapping of rare-earth elements. All rare-earth elements were uniformly distributed without obvious segregation phenomenon, indicating a dual-phase high-entropy LGSEYb with homogeneous compositions could be synthesized by RUHS. Fig. 6(b) shows that mutual aggregation had occurred between the irregular particles, and lattice distortion could be detected at the grain boundaries, with unequal lattice fringes on the two crystal plans. In addition, the lattice fringes with different orientations

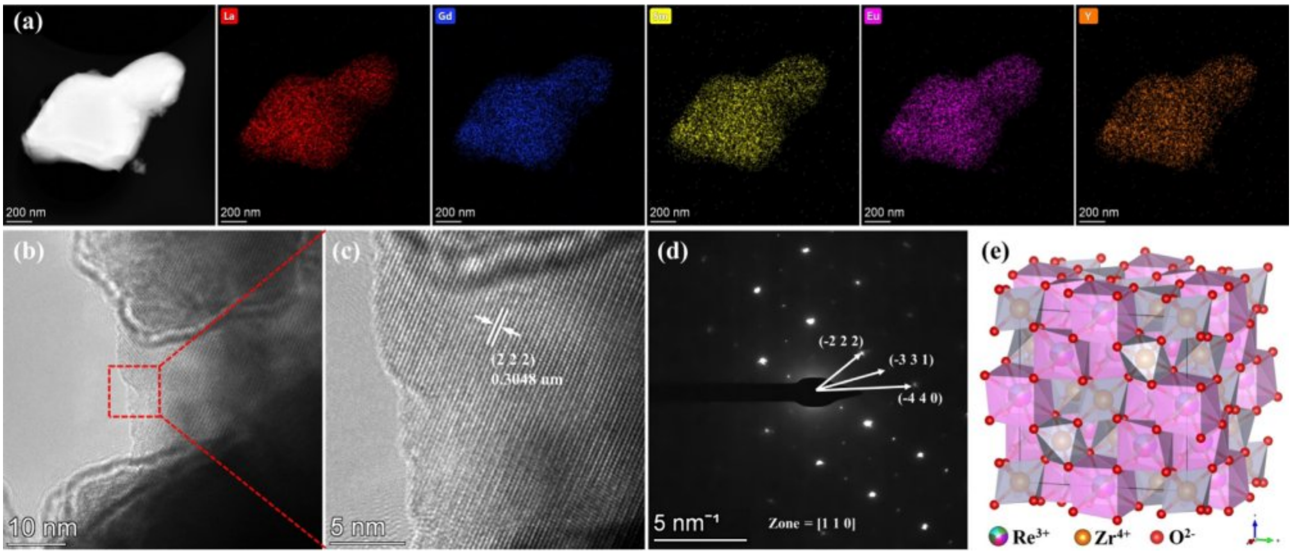

Fig. 5. TEM results of LGSEY. (a) HAADF image and the corresponding TEM-EDS mapping; (b, c) HRTEM of pyrochlore structure; (d) SAED pattern of pyrochlore structure; (e) Crystal structure diagram of pyrochlore structure.

indicated the excellent crystallization of LGSEYb. The SAED pattern results of LGSEYb in Fig. 6(c) demonstrated multiple planes of the dual-phase structure, which were consistent with the XRD results. Fig. 6(d, f) shows lattice stripes of the (220) and (222) planes with calculated planar spacings of 0.186 nm and 0.306 nm, respectively. These lattice stripes were in good agreement with the fluorite structure and the pyrochlore

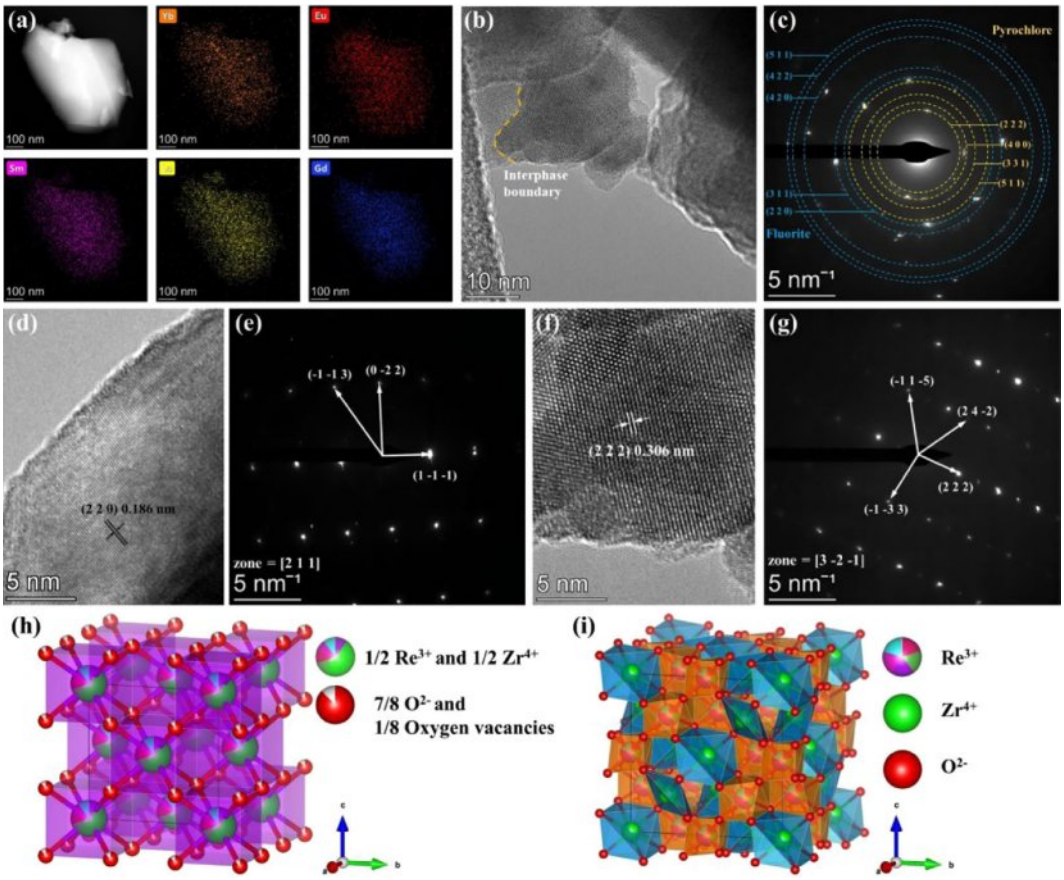

Fig. 6. TEM results of LGSEYb. (a) HAADF image and the corresponding TEM-EDS mapping; (b, c) HRTEM image and the corresponding SAED pattern; (d, e) HRTEM and SAED pattern of fluorite structure; and (f, g) HRTEM and SAED pattern of pyrochlore structure; Crystal structure diagram of (h) fluorite and (i) pyrochlore structure.

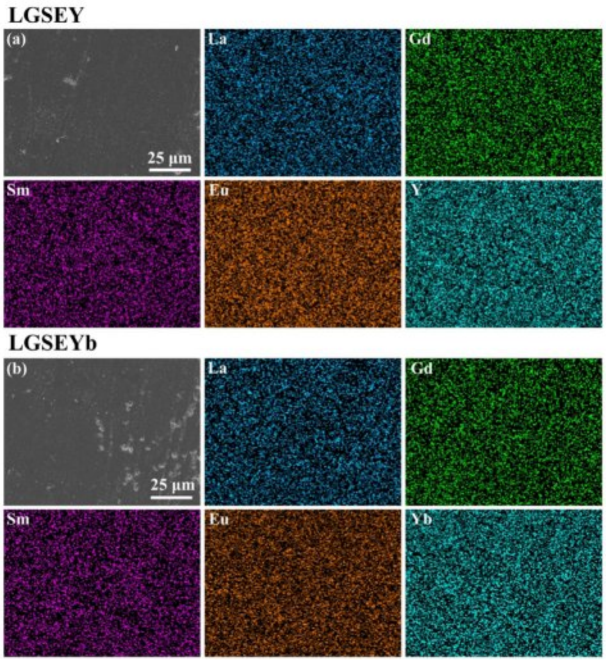

Fig. 7. SEM images and corresponding EDS mapping of (a) LGSEY and (b) LGSEYb.

structure. The SAED pattern of Fig. 6(e, g) confirmed the fluorite and pyrochlore phases had different crystal structures, indicating that LGSEYb was a dual-phase high-entropy ceramic. Fig. 6(h, i) shows the ideal crystal structure of LGSEYb. In the fluorite structure, the cations stochastically dominated the 4a site, and one intrinsic oxygen vacancy was stochastically distributed among every eight 8c oxygen sites. In the pyrochlore structure, the rare-earth cations were homogeneously distributed at the 16d site (1/8, 1/8, 3/8) and coordinated with eight O^{2-} to form the [(La, Gd, Sm, Eu, Yb)O_8], while the Zr^{4+} occupied the 16c site (1/8, 1/8, 1/8) and coordinated with six O^{2-} to form the [ZrO_6] octahedra.

Fig. 7 shows the morphology and the corresponding EDS mapping of LGSEY and LGSEYb. It could be found that the samples prepared by RUHS had a dense morphology without any segregation of rare-earth elements, which confirmed that RUHS could synthesize high-entropy $Re_2Zr_2O_7$ with complex crystal structures and uniform elemental distribution. The actual densities of LGSEY and LGSEYb were measured to be 6.16 and 6.69 g/cm^3 via the Archimedes method, respectively, and the relative density (ρ/ρ_0) of LGSEY and LGSEYb was 98.25% and 96.84%. Compared with traditional solid-state reaction methods, Zhao et al. [8] prepared high-entropy pyrochlore $(La_{0.3}Gd_{0.3}Ca_{0.4})_2(Ti_{0.2}Zr_{0.2}Hf_{0.2}Nb_{0.2}Ta_{0.2})_2O_7$ ceramics by conventional solid-state method at 1600 °C for 4 h, and the relative density of this ceramic is 96%. Luo et al. [38] prepared high-entropy fluorite $(Yb_{0.2}Nd_{0.2}Sm_{0.2}Eu_{0.2}Gd_{0.2})_2Zr_2O_7$ ceramics by conventional solid-state method at 1600 °C for 10 h, and the relative density of this ceramic is 95.75%. Zhang et al. [22] prepared $(La_{0.2}Gd_{0.2}Y_{0.2}Sm_{0.2}Ce_{0.2})_2Zr_2O_7$ by the conventional solid-state method at 1550 °C for 10 h, and the relative density of this ceramic is 95%. Therefore, it can be demonstrated that RUHS can prepare high-entropy $Re_2Zr_2O_7$ with a dense structure.

Thermal conductivity

Thermal conductivity is the most critical parameter of TBC materials. Under identical conditions, lower thermal conductivity in ceramic materials is more beneficial for increasing the operating temperature of the TBCs. Fig. 8(a) illustrates the specific heat capacity (C_p) of LGSEY, LGSEYb, and compares with $La_2Zr_2O_7$ (LZO). It had been observed that the C_p of all materials increased with the temperature rising and approached the limiting value in high-temperature environments. The changing behavior of C_p was related to the lattice vibrations, which could be expressed as follows [39]:

$$C_{mol} = 9R\left(\frac{T}{\theta_D}\right)^3 \int_0^{\theta_D/T} \frac{u^4 e^u}{\left(e^u - 1\right)^2} \mathrm{d}u \qquad (5)$$

where C_{mol} is the molar specific heat capacity, T is the environment temperature, R is a material-related constant,

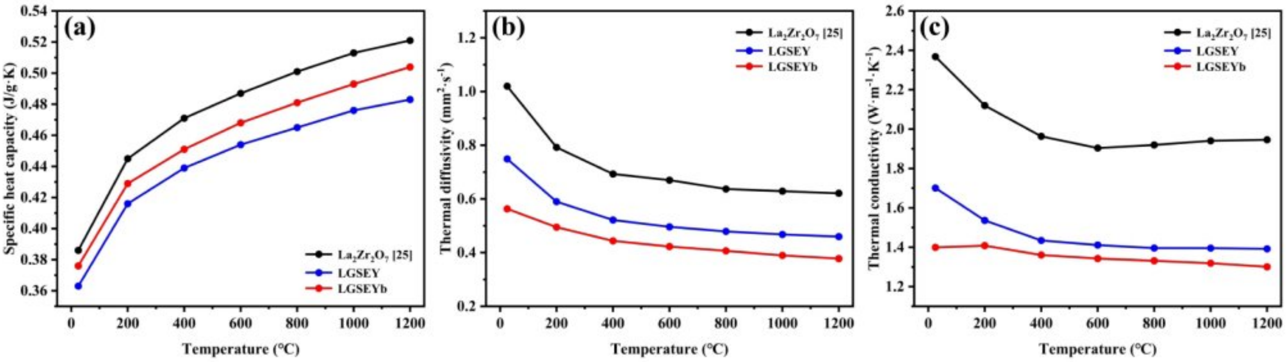

Fig. 8. (a) Specific heat capacity, (b) thermal diffusivity, and (c) thermal conductivity of LGSEY, LGSEYb, and compare with $La_2Zr_2O_7$ [25].

and θ_D is the Debye temperature, respectively. Therefore, the specific heat capacity of LGSEY and LGSEYb ceramics was proportional to T^3 at low temperatures and tended to a limiting value of $3R$ as the temperature increased. The thermal diffusivity of LGSEY and LGSEYb is presented in Fig. 8(b) and compared with LZO. The thermal diffusivity of LGSEY and LGSEYb at 25 °C was 0.75 and 0.54 mm^2/s, respectively, much lower than those of LZO (1.04 mm^2/s). Furthermore, the thermal diffusivity of all ceramic materials decreased with increasing temperature from 25-1200 °C, consistent with the trend that thermal diffusivity was inversely proportional to temperature. The thermal diffusivity of all materials tended to a limiting value with increasing temperature, which was related to the phonon scattering behavior within the ceramic material [40]. Fig. 8(c) shows the thermal conductivity of all materials calculated based on Eq. (1). The calculated thermal conductivity of LGSEY and LGSEYb at 25 °C was only 1.70 and 1.39 $W \cdot m^{-1} \cdot K^{-1}$, respectively, which was much smaller than $La_2Zr_2O_7$ (2.41 $W \cdot m^{-1} \cdot K^{-1}$, 25 °C). In addition, the thermal conductivity of LZO and LGSEY displayed a 1/T dependence on temperature and exhibited a polycrystalline thermal behavior, indicating the phonon scattering was achieved by anharmonic atomic vibrations. In addition, the LGSEYb demonstrated an amorphous thermal conductivity in the entire temperature range, as characterized by only slight variations in thermal conductivity with the rising temperature (1.30-1.41 $W \cdot m^{-1} \cdot K^{-1}$, 25-1200 °C).

The amorphous thermal conductivity of LGSEYb was related to the co-existing pyrochlore and fluorite structure. In particular, there was a significant ionic radius difference between the different rare-earth cations within the dual-phase LGSEYb, which could reach 17.8%. The radius difference increased the crystal structure disorder, enhanced the distortion degree of the anionic sublattice, and changed the position of the oxygen ions. Two types of oxygen vacancies existed within dual-phase LGSEYb: The first was a randomly distributed oxygen vacancy in the fluorite structure, and the second was an oxygen vacancy with a specific position in the pyrochlore structure. The two types of oxygen vacancies led to a thermal conductivity similar to amorphous materials.

During the engineering process of high-entropy $Re_2Zr_2O_7$, the large atomic mass and size differences introduced by rare-earth cations will lead to higher nonlinear vibrations, which will reduce the phonon mean free path and further enhance the scattering effect between phonons, resulting in lower thermal conductivity [41]. According to Clark's design theory for low thermal conductivity ceramic materials, phonon scattering is the dominant thermal conduction mechanism, and the point defects induced by substitutional cations will be favorable for reducing phonon mean free path. Generally, the relaxation time (τ) and phonon scattering can be expressed as follows [42]:

$$\frac{1}{\tau_C}=\frac{1}{\tau_U}+\frac{1}{\tau_M}+\frac{1}{\tau_B} \tag{6}$$

where τ_U is the Umklapp scattering, τ_M is the phonon scattering due to point defects in ceramic materials, and τ_B is the phonon scattering at the grain boundaries of the ceramic particles. Generally, the grain size of ceramics is much larger than the phonon mean free path, so the τ_B can be ignored. Thus, the phonon mean free path (l_p) associated with atomic mass and ionic radius difference can be described as [43]:

$$\frac{1}{l_p}=\frac{\alpha^3}{4\pi v^4}\omega^4 c\left(\frac{\Delta M}{M}\right)^2 \tag{7}$$

$$\frac{1}{l_p}=\frac{2\alpha^3\omega^4 c}{4\pi v^4}J^4\gamma^2\left(\frac{\Delta R}{R}\right)^2 \tag{8}$$

where α^3, v, ω, c, M, J, γ, and R represents atomic volume, the transverse acoustic velocity, the phonon frequency, the point defect concentration, the average atomic mass, a constant, the Grunesien parameter, and average ionic radius, respectively. Since the large atomic mass and radius differences in high-entropy $Re_2Zr_2O_7$ are the main factors affecting the thermal conductivity, to more accurately characterize the low thermal conductivity of LGSEY and LGSEYb, mass disorder ($\Delta M/M$) and size disorder ($\Delta R/R$) are used as descriptors for the calculations, which can be calculated as follow:

$$\frac{\Delta M}{M}=\frac{\sqrt{\sum_{i=1}^{n}c_i\left(M_i-\sum_{i=1}^{n}c_iM_i\right)^2}}{\sum_{i=1}^{n}c_iM_i} \tag{9}$$

$$\frac{\Delta R}{R}=\frac{\sqrt{\sum_{i=1}^{n}c_i\left(R_i-\sum_{i=1}^{n}c_iR_i\right)^2}}{\sum_{i=1}^{n}c_iR_i} \tag{10}$$

where n is the atom number, c_i, M_i, and R_i represent the molar content, atomic mass, and ionic radius of the i-th element, respectively. According to the atomic masses and Shannon ionic radius listed in Table 1, the $\Delta M/M$ ($\Delta R/R$) of LGSEY, LGSEYb, and LZO was 0.975 (0.218), 1.003 (0.219), and 0.956 (0.209), respectively. The above studies demonstrate that higher mass and size disorder contribute to phonon scattering and decrease thermal conductivity.

Mechanical properties

During the application of thermal barrier coatings, the mechanical properties of the ceramic material will directly affect the performance of the coating system. Table 3 lists the V_T, V_L, and E of LGSEY and LGSEYb.

Table 3. The acoustic velocity (V_L and V_T) and Young's modulus (E) of LGSEY and LGSEYb.

Compounds	V_L (m·s^{-1})	V_T (m·s^{-1})	E (GPa)
LGSEY	6541	3672	210.96
LGSEYb	6177	3424	200.51

The V_L and V_T of LGSEYb were 6177 and 3424 m·s^{-1}, respectively, lower than those of LGSEY, indicating LGSEYb exhibited a weak interatomic bonding strength. Fig. 9 shows the mechanical properties of LGSEY, LGSEYb, and compare with LZO. The hardness of LGSEY and LGSEYb was 12.45 and 11.94 GPa, respectively, which was higher than that of LZO (9.42 GPa). Generally, the hardness of ceramic materials is affected by several factors, including crystal structure, defects, atomic mass, and size differences [40, 44]. First, the mass and size differences between the different cations result in superior hardness by generating impedance mismatch reflections and energy generated by terminal dislocation motion. Second, LGSEY and LGSEYb contain six types of cations. According to Table 1, the cation radius difference of LGSEY and LGSEYb could be up to 45%, which led to severe lattice distortion of the sublattice. Both energy scattering mechanisms enhanced the mechanical work required for the plastic deformation of LGSEY and LGSEYb, ultimately increasing the hardness of both materials [45]. Fracture toughness is another important property of ceramic materials that determines the reliability of TBCs. The fracture toughness of LGSEY and LGSEYb was 1.48 and 1.45 MPa·m$^{1/2}$, which was higher than $La_2Zr_2O_7$ (1.20 MPa·m$^{1/2}$) but still lower than YSZ (2.64 MPa·m$^{1/2}$). The relatively low fracture toughness of LGSEY and LGSEYb might be related to the faster heating and cooling rates during the RUHS process, which increases the thermal stresses within the ceramic material [46]. Therefore, the fracture toughness of LGSEY and LGSEYb needs to be further optimized.

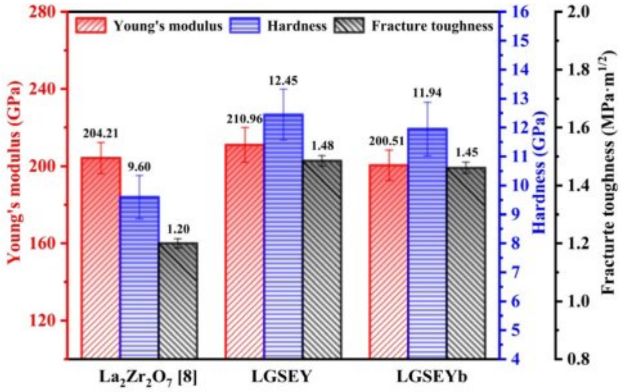

Fig. 9. Young's modulus (E), hardness (H_V), and fracture toughness (K_{IC}) of LGSEY, LGSEYb, and compare them with $La_2Zr_2O_7$ [8].

Phase stability

High-temperature phase stability is a key performance indicator for the ceramic coat of thermal barrier coatings to resist thermal cycling failure. Under a high-temperature environment, the metastable tetragonal phase of YSZ will decompose into a tetragonal phase and a cubic phase, and the tetragonal phase will be further transformed into a monoclinic phase accompanied by 3-5% volume expansion [47]. Therefore, LGSEY and LGSEYb should have excellent high-temperature phase stability. Fig. 10(a) and (b) show the TG-DSC curves of LGSEY and LGSEYb from room temperature to 1500 °C. During the heating process, the DSC curves of the two ceramic materials did not show obvious endothermic and exothermic peaks, indicating that the two ceramic materials did not undergo phase transformation. In addition, the TG curves of the two materials remained almost constant during the heating process, indicating that the two ceramic materials have excellent high-temperature stability.

Fig. 11 shows the XRD patterns of LGSEY and LGSEYb after calcination at 1500 °C for 50 h. The

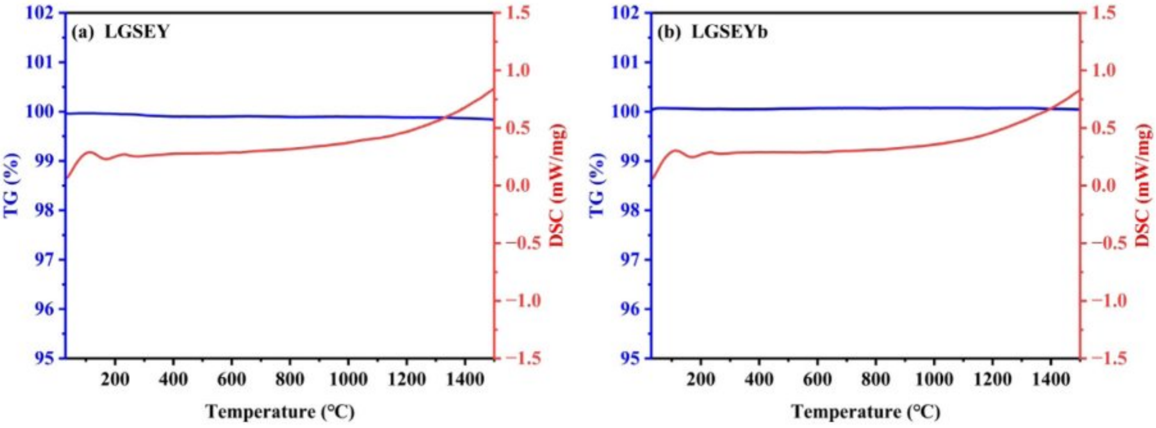

Fig. 10. TG-DSC curves of LGSEY (a) and LGSEYb, (b) from room temperature to 1500 °C.

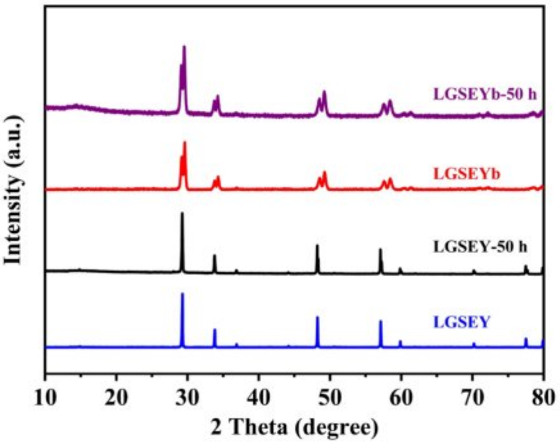

Fig. 11. XRD of LGSEY and LGSEYb samples calcined at 1500 °C for 50 h.

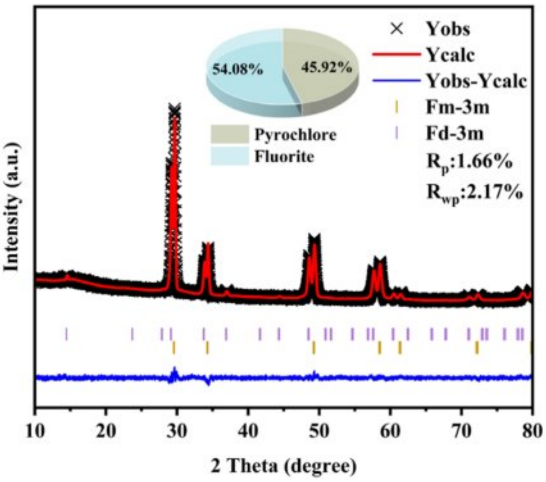

Fig. 12. Rietveld refinement of LGSEYb samples calcined at 1500 °C for 50 h.

comparison reveals that LGSEY still had a single-phase pyrochlore structure, which was consistent with the TG-DSC results, indicating that LGSEY exhibited excellent high-temperature phase stability. For LGSEYb high-entropy ceramics, although the diffraction peaks of the calcined samples were consistent with those of the sintered samples, LGSEYb has a dual-phase structure with the co-existence of pyrochlore and fluorite phases. Thus, the calcined XRD needs to be refined to determine the contents of the two phases. Fig. 12 shows the refinement curve of LGSEYb calcined at 1500 °C for 50 h. The fitting factors R_{wp} and R_p were below 2.17% and 1.66%, respectively, indicating the refinement results were reliable. Based on the refinement results, the LGSEYb was composed of 45.92% pyrochlore phase and 54.08% fluorite phase after calcination. The phase composition of LGSEYb remained almost the same before and after calcination, indicating the LGSEYb exhibited excellent high-temperature phase stability.

Conclusions

In this work, $(La_{0.2}Gd_{0.2}Sm_{0.2}Eu_{0.2}Y_{0.2})_2Zr_2O_7$ and $(La_{0.2}Gd_{0.2}Sm_{0.2}Eu_{0.2}Yb_{0.2})_2Zr_2O_7$ high-entropy ceramics were synthesized via the reactive ultrafast high-temperature sintering. In addition, the phase composition, structural characterization, thermal conductivity, and mechanical properties of the two ceramics were investigated. The results showed that the high-entropy LGSEY with a single-phase structure and high-entropy LGSEYb with a dual-phase structure were successfully synthesized by the RUHS in less than 1 h, indicating the feasibility of the RUHS technique in the preparation of high-entropy $Re_2Zr_2O_7$ with complex structures. In addition, TEM and SEM results showed that high-entropy ceramics with a uniform distribution of rare-earth elements could be synthesized by UHS technology, avoiding the effect of compositional bias on the properties of high-entropy ceramics. In terms of thermal conductivity, both LGSEY and LGSEYb exhibited low thermal conductivity due to the severe lattice distortion, and LGSEYb exhibited an amorphous thermal conductivity behavior. In terms of mechanical properties, both LGSEY and LGSEYb exhibited low Young's modulus and high hardness due to the significant cation radius difference and severe lattice distortion in high-entropy ceramics. In terms of thermal stability, single-phase LGSEY and two-phase LGSEYb exhibit excellent high-temperature phase stability in the range of room temperature to 1500 °C. In summary, single-phase and dual-phase high-entropy $Re_2Zr_2O_7$ with complex structures can be synthesized by UHS and optimized for the internal distribution of rare-earth elements. We expect that this study will be beneficial in optimizing the synthesis of high-entropy $Re_2Zr_2O_7$ and provide a reference for the rapid and efficient synthesis of TBC ceramic materials.

Acknowledgments

This work was supported by the National Nature Science Foundation of China (No. 51702145, 51972155, and 52371066). Educational Commission of Liaoning Province of China (No. FWDF202003 and LJKZ0306).

References

1. J.H. Liu, Y.Y. Wang, Z. Lu, Y.G. Jung, G. Lyu, Y.W. Zhou, J. Zhang, and Y. Li, J. Ceram. Process. Res. 25[5] (2024) 875-903.
2. J.H. Liu, Z. Lu, Y.W. Zhou, J. Zhang, and G.L. Lyu, J. Ceram. Process. Res. 24[2] (2023) 285-307.
3. J.H. Liu, Z. Lu, Y.G. Jung, J.H. Son, G.L. Lyu, Y.Y. Wang, J. Zhang, Y.W. Zhou, and Y. Li, J. Ceram. Process. Res. 25[6] (2024) 1013-1041.
4. D. H. Lee, B. Jang, C. Kim, and K.S. Lee, J. Ceram. Process. Res. 20[5] (2019) 499-504.
5. J.W. Lee, C.H. Lee, and H.J. Kima, J. Ceram. Process.

Res. 2[3] (2001) 113-119.

6. J.B. Huang, W.Z. Wang, Y.J. Li, H.J. Fang, D.D. Ye, X.C. Zhang, and S.T. Tu, Surf. Coat. Technol. 402 (2020) 126304.
7. B. Shreeram, M. Rajeshwaran, S.M. Jinnah, Nandhakumar, and T.C.A. Kumar, J. Ceram. Process. Res. 23[3] (2022) 263-267.
8. Z.F. Zhao, Z.Y. Ruan, R. Li, S.X. Yan, X.L. Sun, C. Liu, D. Zhang, B. Xu, Z.Y. Ren, M. Wang, J.Y. Li, J. Tian, Y.H. Jiang, J. Feng, and Y.C. Zhou, J. Mater. Sci. Technol. 205 (2025) 315-326.
9. J.B. Fan, Q.S. Wang, X.J. Ning, L. Li, and Z.N. Sun, J. Eur. Ceram. Soc. 45[5] (2025) 117089.
10. X.Y. Liu, P. Zhang, Y. Lu, G.H. Liu, J. Sun, W. Liu, W. Pan, and C.L. Wan, Surf. Coat. Technol. 471 (2023) 129928.
11. W. Ma, X.H. Li, X.F. Meng, Y.N. Xue, Y. Bai, W.D. Chen, and H.Y. Dong, J. Therm. Spray Technol. 27[7] (2018) 1056-1063.
12. H. Yao, D.L. Shan, K. Pan, S.H. Xie, Z.J. He, C.H. Lei, and Y.Y. Liu, Int. J. Heat Mass Transf. 236 (2025) 126268.
13. J. Wang, X.Y. Chong, R. Zhou, and J. Feng, Scr. Mater. 126 (2017) 24-28.
14. K.Y. Lue, S.J. Dong, Y. Huang, C.Y. Mao, J.N. Jiang, L.H. Deng, and X.Q. Cao, Surf. Coat. Technol. 443 (2022) 128594.
15. L. Guo, Y. Zhang, X.X. Zhao, C.M. Wang, and F.X. Ye, Ceram. Int. 42[1] (2016) 583-588.
16. X.W. Luo, R.Q. Huang, C.H. Xu, S. Huang, S. Hou, and H.Y. Jin, J. Alloys Compd. 926 (2022) 166714.
17. J.W. Yeh, S.K. Chen, J.Y. Gan, S.J. Lin, T.S. Chin, T.T. Shun, C.H. Tsau, and S.Y. Chang, Metall. Mater. Trans. A 35A[8] (2004) 2533-2536.
18. C.M. Rost, E. Sachet, T. Borman, A. Moballegh, E.C. Dickey, D. Hou, J.L. Jones, S. Curtarolo, and J.P. Maria, Nat. Commun. 6 (2015) 8485.
19. W.L. Hsu, C.W. Tsai, A.C. Yeh, and J.W. Yeh, Nat. Rev. Chem. 8[6] (2024) 471-485.
20. M.H. Tsai and J.W. Yeh, Mater. Res. Lett. 2[3] (2014) 107-123.
21. S. Fu, Z.J. Jia, D.T. Wan, and Y.W. Bao, Ceram. Int. 50[3] (2024) 5510-5515.
22. D.B. Zhang, N. Wang, R.Q. Song, and M.L. Zhou, Ceram. Int. 50[1] (2024) 2490-2500.
23. Y.H. Wang, Y.J. Jin, T. Wei, Z.G. Wang, G. Cao, Z.Y. Ding, Z.G. Liu, J.H. Ouyang, Y.J. Wang, and Y.M. Wang, J. Alloys Compd. 918 (2022) 165636.
24. J.T. Zhu, X.Y. Meng, P. Zhang, Z.L. Li, J. Xu, M.J. Reece, and F. Gao, J. Eur. Ceram. Soc. 41[4] (2021) 2861-2869.
25. W.W. Shuai, W. Qian, Z.C. Guan, Z.B. Li, Y.Q. Hua, and J. Cai, Ceram. Int. 50[7] (2024) 10525-10534.
26. C.W. Wang, W.W. Ping, Q. Bai, H.C. Cui, R. Hensleigh, R.L. Wang, A.H. Brozena, Z.P. Xu, J.Q. Dai, Y. Pei, C.L. Zheng, G. Pastel. J.L Gao, X.Z. Wang, H. Wang, J.C. Zhao, B. Yang, X.Y. Zheng, J. Luo, Y.F. Mo, B. Dunn, and L.B. Hu, Science 368[6490] (2020) 521-526.
27. L. Karacasulu, T.H. de Beauvoir, E. De Bona, M. Cassetta, C. Vakifahmetoglu, V.M. Sglavo, M. Bortolotti, C. Manière, C. Estournès, and M. Biesuz, J. Eur. Ceram. Soc. 45[2] (2025) 116879.
28. X. Zhao, W.T. Wu, Y.H. Bai, Y.H. Wu, J. Liu, P.P. Wang, H. Luo, K. Ren, Y. Song, H.L. Du, and J. Deng, J. Power Sources 613 (2024) 234913.
29. B.W. Zhang, M.C. Hu, F.G. Zhong, S.P. Zhang, Z.W. Yang, X.C. Qiu, J.B. Xu, O.Y. Jun, Y. Zhang, B.P. Zhu, X.F. Yang, and S. Chen, J. Eur. Ceram. Soc. 44[10] (2024) 5569-5578.
30. Q.Q. Li, H.L. Du, X. Zhao, F. Zhao, Y.C. Zhang, X.J. Hu, and X. Du, Ceram. Int. 50[11] (2024) 18907-18914.
31. M. Kermani, C.F. Hu, and S. Grasso, Ceram. Int. 49[3] (2023) 4017-4029.
32. S.Q. Wu, Z.L. Xue, X.J. Ji, E.S. Byon, and S.H. Zhang, J. Alloys Compd. 842 (2020) 155872.
33. Y. Ma, X.B. Zhao, F.Y. Hong, and K. Yang, Ceram. Int. 50[23] (2024) 51410-51420.
34. X.W. Luo, S. Huang, R.Q. Huang, C.H. Xu, S. Hou, and H.Y. Jin, Ceram. Int. 49[14] (2023) 23410-23416.
35. W. Fan, Y. Bai, Y.F. Liu, T.T. Li, B.M. Li, L. Zhang, C.M. Gao, S.Y. Shan, and H.C. Han, J. Mater. Sci. Technol. 107 (2022) 149-154.
36. H.B. Yang, G.Q. Li, H.P. Bu, H.J. Liu, L.X. Yang, W.J. Wang, X.H. Lin, C. Fu, Y.S. Wang, and C.L. Zeng, Ceram. Int. 48[5] (2022) 6956-6965.
37. H.M. Zhang, Y. Song, W.W. Sang, Y.H. Guo, Y.K. Zhao, Y.Z. Zhao, S. Song, C.M. Li, R.T. Li, Z.Z. Li, H.S. Zhang, X.L. Zhang, and X.G. Chen, Ceram. Int. 48[6] (2022) 8380-8386.
38. X.W. Luo, L.R. Luo, X.F. Zhao, H.Y. Cai, S.S. Duan, C.H. Xu, S. Huang, H.Y. Jin, and S. Hou, J. Eur. Ceram. Soc. 42[5] (2022) 2391-2399.
39. D. Abdullah, and D.C. Gupta, Sci. Rep. 14[1] (2024) 26168.
40. D. Song, T. Song, U. Paik, G. Lyu, Y.G. Jung, H.B. Jeon, and Y.S. Oh, Mater. Des. 210 (2021) 110059.
41. W.W. Sang, H.S. Zhang, H.H. Chen, B. Wen, and X.C. Li, J. Inorg. Mater. 36[4] (2021) 405-410.
42. G.F. Xie, Y.L. Shen, X.L. Wei, L.W. Yang, H.P. Xiao, J.X. Zhong, and G. Zhang, Sci. Rep. 4 (2014) 5085.
43. X.W. Luo, L.R. Luo, X.F. Zhao, H.Y. Cai, S.S. Duan, C.H. Xu, S. Huang, H.Y. Jin, and S. Hou, J. Eur. Ceram. Soc. 42[5] (2022) 2391-2399.
44. T.J. Harrington, J. Gild, P. Sarker, C. Toher, C.M. Rost, O.F. Dippo, C. McElfresh, K. Kaufmann, E. Marin, L. Borowski, P.E. Hopkins, J. Luo, S. Curtarolo, D.W. Brenner, and K.S. Vecchio, Acta Mater. 166 (2019) 271-280.
45. P. Sarker, T. Harrington, C. Toher, C. Oses, M. Samiee, J.P. Maria, D.W. Brenner, K.S. Vecchio, and S. Curtarolo, Nat. Commun. 9 (2018) 4980.
46. Z. Teng, P. Wang, S.F. Zeng, W.L. Feng, C. Chen, P. Jia, Y.Q. Tan, and S.M. Peng, Ceram. Int. 50[4] (2024) 6892-6897.
47. G. Lyu, I.S. Kim, D. Song, H.M. Park, J.S. Kim, T. Song, S. Myoung, Y.G. Jung, and J. Zhang, Ceram. Int. 46[2] (2020) 1307-1313.